

# Transparent Conductive Oxide Sputtering Damage on Contact Passivation in Silicon Heterojunction Solar Cells with Hydrogenated Nanocrystalline Silicon

Depeng Qiu, Weiyan Duan,\* Andreas Lambertz, Alexander Eberst, Karsten Bittkau, Uwe Rau, and Kaining Ding

Mitigating the adverse effect of transparent conductive oxide (TCO) sputtering on the passivation quality of the heterojunction contact is very critical for achieving high-efficiency silicon heterojunction (SHJ) solar cells. Herein, n-type ultra-thin (5 nm) nanocrystalline silicon (nc-Si:H) is utilized as a contact layer in rear-junction SHJ solar cells. It is revealed that the TCO sputtering damage on the contact layer is caused by the ion bombardment during the sputtering process and cannot be fully recovered by low-temperature annealing. A more severe passivation deterioration is observed for the devices with nc-Si:H(n) having a higher microstructure factor. This result is explained by an increased ion penetration depth in the porous nc-Si:H film. By applying denser nc-Si:H(n) in SHJ solar cells, the front silicon film stack shows more resilience to sputter damage, yielding a remarkable cell performance on the M2-size wafer with certificated power conversion efficiency ( $\eta$ ) of 23.87%. The sputter damage on nc-Si:H by TCO in SHJ solar cells is explored in depth for the first time from the perspective of silicon thin films.

silicon (nc-Si:H) film was used as the contact layer.<sup>[3]</sup> The nc-Si:H is a mixture of materials with crystalline silicon phases embedded in an amorphous silicon (a-Si:H) matrix.<sup>[1,4–6]</sup> Due to the higher doping efficiency in the crystalline phase, its dark conductivity can be up to two orders of magnitude higher than that of the doped a-Si:H, which is beneficial for the improvement of fill factor (FF) in SHJ solar cells.<sup>[7–11]</sup> The thickness of the doped layer in high-efficiency SHJ solar cells is usually maintained below 10 nm to avoid too much parasitic absorption in the front layers. Besides, using a thin layer for devices is essential to bring the production cost down, especially in terms of the processing time and the material consumption. However, it is a big challenging task to prepare the thin nc-Si:H layer with-

out compromising their electronic properties.<sup>[4,7,12]</sup> In addition, the thin nc-Si:H/a-Si:H stack should be able to withstand the sputtering damage from the transparent conductive oxide (TCO) sputtering process.<sup>[2,13]</sup> The sputter damage from energetic ion bombardment or luminescence of the sputter plasma can lead to deterioration of passivation at the a-Si:H/c-Si interface.<sup>[2,13–15]</sup> Thus, avoiding the detrimental effects of TCO depositions on underlying nc-Si:H/a-Si:H layers is very critical for achieving high-efficiency SHJ solar cells.

To eliminate the passivation degradation during sputtering, many methods were proposed and developed, such as using soft atomic layer deposition (ALD) instead of sputtering,<sup>[16–18]</sup> reducing the initial energy of ions by decreasing sputtering power density or increasing the process pressure,<sup>[19,20]</sup> and softly pre-depositing protective TCO layer against subsequent sputter-deposition.<sup>[20,21]</sup> Most of these methods are related to the adjustment of the TCO deposition conditions. However, the strategies associated with the optimization of the doped layer properties are not often investigated in detail, especially for the SHJ cells with an nc-Si:H thin film.


In this article, ultra-thin ( $\approx 5$  nm) phosphorus doped nc-Si:H (nc-Si:H(n)) layers were utilized as contact layer in rear-junction SHJ solar cells. We first discussed the differences in the sputtering effect between devices with nc-Si:H(n) layers prepared at various deposition parameters. Second, the link between the sputtering damage and the optoelectronic properties of

## 1. Introduction

Owing to the excellent surface passivation, the low-temperature process, and the lean fabrication steps, silicon heterojunction (SHJ) solar cells have triggered more and more attention both in the academic field and photovoltaic industry over the past few years.<sup>[1,2]</sup> Recently, a world-record power conversion efficiency ( $\eta$ ) of 26.5% was demonstrated for a both-side contacted SHJ solar cell, in which the n-type hydrogenated nanocrystalline

D. Qiu, W. Duan, A. Lambertz, A. Eberst, K. Bittkau, U. Rau, K. Ding  
IEK-5 Photovoltaics  
Forschungszentrum Jülich GmbH  
52425 Jülich, Germany  
E-mail: w.duan@fz-juelich.de

D. Qiu, A. Eberst, U. Rau  
Faculty of Electrical Engineering and Information Technology  
RWTH Aachen University  
52074 Aachen, Germany

 The ORCID identification number(s) for the author(s) of this article can be found under <https://doi.org/10.1002/solr.202200651>.

© 2022 The Authors. Solar RRL published by Wiley-VCH GmbH. This is an open access article under the terms of the Creative Commons Attribution-NonCommercial-NoDerivs License, which permits use and distribution in any medium, provided the original work is properly cited, the use is non-commercial and no modifications or adaptations are made.

DOI: 10.1002/solr.202200651

nc-Si:H(n) layers was revealed and established. Third, a strategy to reduce the sputtering damage was developed and the corresponding devices were fabricated to assess its validity.

## 2. Experimental Section

The nc-Si:H(n) films in this work were prepared in a plasma-enhanced chemical vapor deposition (PECVD) system from Meyer Burger and the precursor gases are silane ( $\text{SiH}_4$ ), hydrogen ( $\text{H}_2$ ), and phosphine ( $\text{PH}_3$ , 1% diluted in  $\text{H}_2$ ). The gas composition is defined by the ratios:  $f_{\text{PH}_3} = [\text{PH}_3]/([\text{PH}_3] + [\text{SiH}_4])$  and  $f_{\text{SiH}_4} = [\text{SiH}_4]/([\text{H}_2] + [\text{SiH}_4])$ , where the  $[\text{H}_2]$ ,  $[\text{PH}_3]$ , and  $[\text{SiH}_4]$  are the gas mass flow rate of  $\text{H}_2$ ,  $\text{PH}_3$ , and  $\text{SiH}_4$ , respectively. The plasma excitation frequency of the generator was set at 13.56 MHz and the substrate temperature was fixed at 200 °C. For material characterization, nc-Si:H(n) films with a thickness of  $\approx 35$  nm were deposited on glass (1.1 mm, Corning Eagle 2000) and double-side polished wafers (525  $\mu\text{m}$ , p-type, 10–20  $\Omega\text{cm}$ ), where 6 nm intrinsic a-Si:H (a-Si:H(i)) was pre-deposited. The thickness of the films and the refractive index ( $n$ ) was determined by spectroscopic ellipsometry (SE) from J. A. Woollam M-2000. UV Raman scattering spectroscopy was performed to determine the fraction of crystallites ( $F_c$ ) in the nc-Si:H films.<sup>[22]</sup> The lateral dark conductivity ( $\sigma$ ) of the films was measured by two coplanar silver electrodes at room temperature. The transmittance  $T$  and reflectance  $R$  were characterized by a dual beam photo spectrometer Lambda 950 in the wavelength range of 300–1300 nm, from which the absorption coefficient ( $\alpha$ ) was calculated. The optical bandgap ( $E_{04}$ ) was determined at the photon energy, where the absorption coefficient reaches  $10^4\text{ cm}^{-1}$ . To characterize the microstructure of these films, Fourier transform infrared spectroscopy (FTIR) in a Nicolet 5700 system with the wavenumber range between 400 and 4000  $\text{cm}^{-1}$  was used.

For the fabrication of solar cells, 165  $\mu\text{m}$  textured n-type M2 (244  $\text{cm}^2$ ) sized Czochralski silicon wafers from LONGi company with a resistivity of  $0.3 \approx 2.1\ \Omega\text{cm}$  were used. Ozone cleaning procedure and dipping in 1% hydrofluoric (HF) acid were carried out for the wafers, followed by the PECVD depositions of front and rear side silicon stacks. Afterward, 70 nm indium tin oxide (ITO) layers were prepared on each side of the wafer at a substrate temperature of 200 °C by direct current magnetron sputtering. Subsequently, the Ag fingers were screen printed on both sides of the solar cells, followed by annealing treatment at 170 °C for 40 mins. The cross-section structure of the rear-junction solar cells is sketched in **Figure 1**.

The passivation quality in terms of effective lifetime, implied open-circuit voltage ( $iV_{oc}$ ), and implied fill factor ( $iFF$ ) was quantified by quasi-steady-state photo conductance (QSSPC) Sinton WTC-120 in transient mode.<sup>[23]</sup> The front total contact resistivity was determined by the transfer-length method (TLM) with a specific pattern, details of which can be found in ref. [24,25] To evaluate the solar cells performance, current–voltage ( $J$ – $V$ ) characteristics were measured under standard test conditions (AM1.5, 25 °C, and 100  $\text{mW cm}^{-2}$ ) by the LOANA system from pv-tools with a Wavelabs Sinus 220 light source. The external quantum efficiency (EQE) and reflectance ( $R$ ) were measured on a  $20 \times 20\text{ mm}^2$  area of the cells with grids

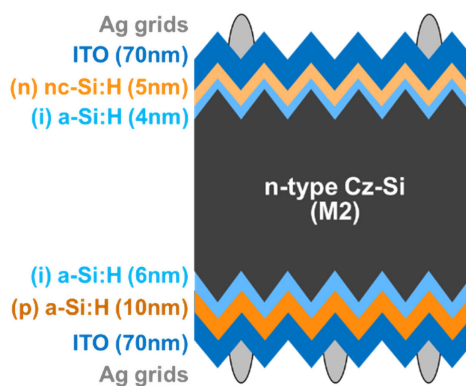


**Figure 1.** The cross-section structure of the rear-junction solar cells with n-type nc-Si:H thin films.

inside. The series resistance ( $R_s$ ) was extracted from a set of  $J$ – $V$  curves obtained at different illumination intensities and the pseudo fill factor ( $pFF$ ) was determined by short-circuit current versus open-circuit voltage ( $I_{sc}$ – $V_{oc}$ ) measurements.<sup>[23]</sup>

## 3. Result and Discussion

### 3.1. Material Properties

The optical and electrical properties of nc-Si:H(n) layers can be adjusted by tuning the deposition parameters, such as the silane gas fraction ( $f_{\text{SiH}_4}$ ), phosphine gas fraction ( $f_{\text{PH}_3}$ ), and power density ( $P$ ).<sup>[26]</sup> In this work, two kinds of nc-Si:H(n) films, namely F1 and F2, were produced, the deposition parameters and opto-electronical properties of which are listed in **Table 1**. By reducing  $f_{\text{SiH}_4}$  from 0.75% to 0.5%, decreasing  $P$  from 200 W to 100 W and increasing  $f_{\text{PH}_3}$  from 2% to 4%, a more conductive and crystalline nc-Si:H(n) film is obtained with a slightly higher bandgap and lower reflective index. Afterward, we applied these two kinds of films (5 nm) in SHJ solar cells as a contact layer, namely D1 and D2, respectively.

### 3.2. Cell Performance

The effective carrier lifetime ( $\tau_{eff}$ ) of the D1 and the D2 before and after the ITO sputtering process is illustrated in **Figure 2a**. There is no noticeable difference between the lifetime curves of the two samples before the ITO deposition, reaching  $\tau_{eff}$  of 3.7 ms at the minority carrier density of  $10^{15}\text{ cm}^{-3}$ . After the ITO deposition, a drop in lifetime curve can be observed in **Figure 2a**, especially for the D2 from 3.8 to 1.4 ms, which is much more severe than the D1. The difference in the passivation degradation between the D1 and the D2 reveals that the sputtering damage could be affected by the properties of nc-Si:H(n) layers. The

**Table 1.** Deposition parameters and opto-electronical properties of two kinds of nc-Si:H(n) layers, named F1 and F2, at thickness of  $\approx 35$  nm with 6 nm a-Si:H(i) underneath.

	$f_{\text{SiH}_4}$ [%]	$P$ [W]	$f_{\text{PH}_3}$ [%]	$p$ [mbar]	$\sigma$ [ $\text{S cm}^{-1}$ ]	$F_c$ [%]	$E_{04}$ [eV]	$n@632\text{ nm}$
F1	0.75	200	2	2.5	0.9	49	2.01	3.98
F2	0.50	100	4	2.5	27	63.5	2.03	3.82

$iV_{oc}$  and  $iFF$  of the samples before and after ITO depositions are plotted in Figure 2b,c, respectively. The  $iV_{oc}$  and  $iFF$  of both samples are similar before the ITO depositions, achieving 740 mV and 86.1%, respectively. After ITO depositions about 5 mV reduction of  $iV_{oc}$  can be noted for the D2, while the  $iV_{oc}$  of the D1 is almost the same as before. Nevertheless, the  $iFF$  degradation of the D1 (1%<sub>abs</sub>) is much less than that of the D2 (3%<sub>abs</sub>).

**Figure 3** shows the cell performance of the solar cells with different nc-Si:H(n) as contact layers. Compared to the D1, a lower  $V_{oc}$  and  $pFF$  are obtained for the D2, which is consistent with the trend of  $iV_{oc}$  and  $iFF$  after ITO deposition mentioned in Figure 2. This result illustrates that the deterioration of the passivation for the D2 during the sputtering process cannot be fully recovered by the annealing treatment after screen printing. Around  $0.1 \text{ mA cm}^{-2}$  reduction of  $J_{sc}$  is obtained for the D2 compared with the D1, which is due to the lower internal quantum efficiency (IQE) in the wavelength range between 600 and 1000 nm as shown in Figure S1 (Supporting Information). It could be interpreted by the worse carrier collection related to the passivation issue in the D2.<sup>[27]</sup> A decreased gap between the  $pFF$  and  $FF$  but an increase of  $FF$  from 76% to 79% are observed for the D2 compared with the D1. Even though cells with the F2 exhibit relatively weak resistance to sputtering damage, replacing the F1 with the F2 does lead to a decline of the front contact resistivity from 1.3 to  $0.5 \Omega \text{ cm}^2$ , which contributes to the reduction of total series resistance from 1.6 to  $0.9 \Omega \text{ cm}^2$ . Consequently, more than 0.6%<sub>abs</sub> gain of  $\eta$  is achieved, reaching 22.8%, by applying more conductive and crystalline nc-Si:H(n) in SHJ solar cells as a contact layer. However, the irreversible damage to the  $V_{oc}$ ,  $J_{sc}$ , and  $pFF$  of the D2 caused by sputtering damage could still be the limitation of  $\eta$ . Therefore, reducing the sputtering damage is very critical to further improve cell performance above 23%.

### 3.3. Analysis of the Sputtering Damage

According to the previous discussion, a change in the sputter damage behavior can be found when modifying the deposition

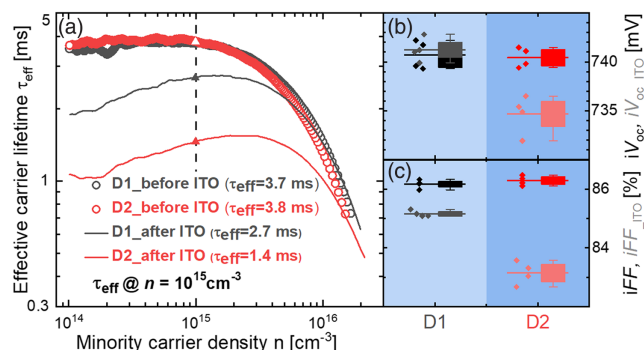


**Figure 2.** a) The effective carrier lifetime ( $\tau_{eff}$ ) versus the minority carrier density ( $n$ ), b) the implied open-circuit voltage ( $iV_{oc}$ ), and c) the implied fill factor ( $iFF$ ) of the precursor devices of the D1 and the D2 were evaluated by the quasi-steady-state photo conductance (QSSPC) lifetime measurement before and after ITO sputtering process. The value of  $\tau_{eff}$  indicated in the graph was determined at the minority carrier density of  $10^{15} \text{ cm}^{-3}$ . The nc-Si:H(n) films (5 nm), named F1 and F2, were used in the D1 and the D2, respectively, the detailed parameters of which are listed in Table 1. The box plots summarize the statistic of 4 samples per group and the line is the median position.

parameters of nc-Si:H(n) layers. To reveal the correlation between the microstructure of nc-Si:H and the sputtering damage, the F1 and F2 were deposited on the a-Si:H(i) coated polished wafer and the corning glass at a device-relevant thickness to evaluate their structural and optical properties.

Uniform silicon layers on the polished wafers can be noted for both samples in Figure S2 (Supporting Information) and their average total thickness is at a similar value, around 13.5 nm. As shown in Figure 4a,b, the F2 is more transparent and with lower absorption coefficient than the F1, which is consistent with the optical band gap listed in Table 1. The IR spectra of the F1 and the F2 in the wavenumber range of  $1800\text{--}2200 \text{ cm}^{-1}$  are displayed in Figure 4c,d, respectively. It can be fitted with two Gaussian-deconvoluted curves, which are the Si-H low stretching mode (LSM) at  $2000 \text{ cm}^{-1}$  and the high stretching mode (HSM) at  $2090 \text{ cm}^{-1}$ ,<sup>[28,29]</sup> marked with different colors. Commonly the Si-H vibration in LSM is associated with the isolated monohydride embedded in dense a-Si bulk and that in HSM is related to the clustered H on the inner surfaces of voids.<sup>[28,29]</sup> The bonded hydrogen content in LSM ( $C_{H}^{LSM}$ ) and HSM ( $C_{H}^{HSM}$ ) can be extracted from the IR spectrum.<sup>[30,31]</sup> It is notable that higher  $C_{H}^{HSM}$  and slightly lower  $C_{H}^{LSM}$  is obtained for the F2 compared with the F1, revealing more voids and less dense structures are generated in the amorphous network of the F2. Consequently, an increased microstructure factor ( $R^*$ ), defined by  $R^* = C_{H}^{HSM} / (C_{H}^{LSM} + C_{H}^{HSM})$ , is found for the F2 in Figure 4f compared with the F1, indicating that the film becomes more porous.<sup>[32–35]</sup> The difference of  $iV_{oc}$  ( $\Delta iV_{oc}$ ) before and after ITO deposition for the devices with different nc-Si:H(n) layers in Ref. [26] is plotted versus the material properties, such as  $F_c$ ,  $\alpha$ ,  $n$  and  $R^*$ , and shown in Figure 5. No noticeable relationship between  $F_c$  and  $\Delta iV_{oc}$  is observed in Figure 5a, while a lower absolute value of  $\Delta iV_{oc}$  is obtained at lower  $R$  and higher  $\alpha$  and  $n$ . This result suggests that the microstructure of the nc-Si:H layers could play a dominant role in the generation of sputter damage.

Evidence from the literature demonstrates that the sputtering damage could be assigned to the luminescence of the sputtering plasma and the ion bombardment during the sputter-deposition of the ITO.<sup>[13–15,20,36,37]</sup> During sputtering, the substrate is exposed to a broad spectrum of radiations, thermal and high-energy electrons, and the atoms/ions of the target material or the process gases.<sup>[38]</sup> The vacuum ultraviolet (VUV) or ultraviolet (UV) radiations related to the oxygen or Argon plasma could induce metastable defects in the a-Si:H bulk or the wafer surface, such as the dangling bonds, causing a deterioration of the surface passivation. An excess of charge carriers or electron-hole pairs in the silicon film could be excited by the secondary electron emission or the ionization energy provided by the ion neutralization process. These energetic excess carriers would facilitate the emission of H and the breakage of the Si-H bonds in a-Si:H(i) or on c-Si surface, causing the deterioration of the surface passivation.<sup>[14,39–41]</sup> It was demonstrated that the F2 is more transparent and porous than the F1, as shown in Figure 4. Thus, two possibilities could be responsible for the worse passivation obtained in the D2. One is the increased transparency of the silicon layers, which lets more VUV or UV photons reach the passivation layer or the wafer surface,

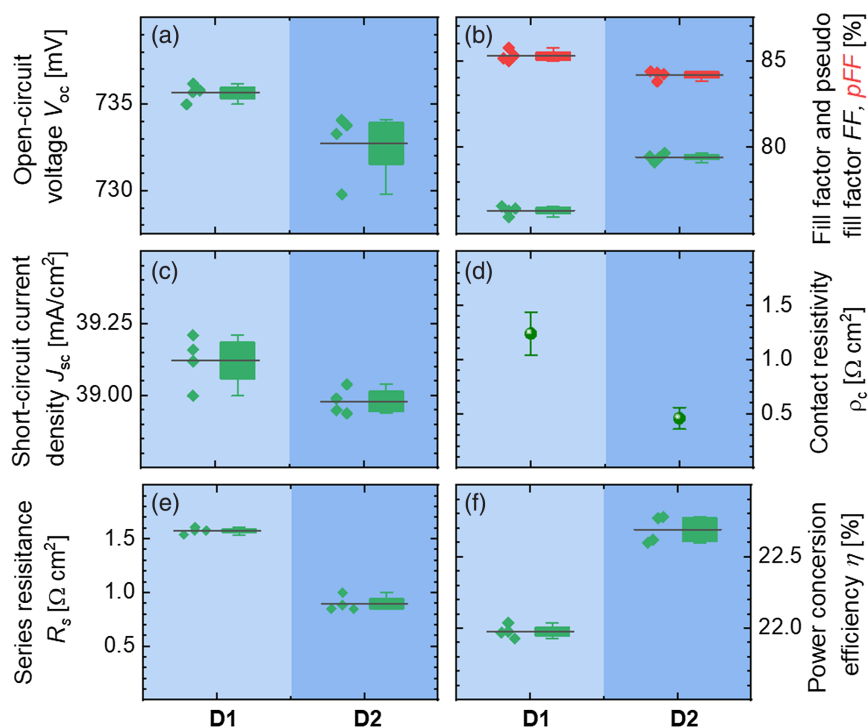


**Figure 3.** a) Open-circuit voltage ( $V_{oc}$ ), b) fill factor (FF) and pseudo fill factor ( $pFF$ ), c) short-circuit current density ( $J_{sc}$ ), d) front total contact resistivity ( $\rho_c$ ), e) series resistance ( $R_s$ ), and f) power conversion efficiency ( $\eta$ ) of the solar cells, named D1 and D2. The nc-Si:H(n) films, namely F1 and F2, were used in the D1 and the D2, respectively, the detailed parameters of which are listed in Table 1. The box plots summarize the statistic of 4 samples per group and the line is the median position.

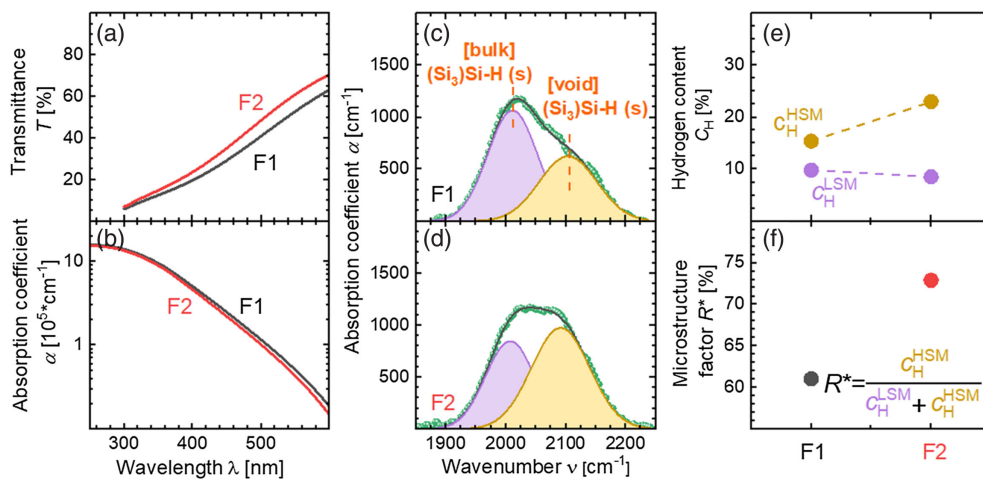


**Figure 4.** a) The transmittance ( $T$ ) and b) absorption coefficient ( $\alpha$ ) of the a-Si:H(i)/nc-Si:H(n) stacks as a function of the wavelength. c,d) Deconvolution of the IR absorption spectrum for the a-Si:H(i)/nc-Si:H(n) stacks into Si-H low stretching mode (LSM) and high stretching mode (HSM). The vertical dash lines define the position of LSM and HSM. e) The hydrogen content  $C_H^{LSM}$ ,  $C_H^{HSM}$  and f) microstructure factor  $R^*$  estimated from the equation indicated in the graph. The F1 and F2 correspond to the recipe used for nc-Si:H(n) layers, details of which are listed in Table 1.

yielding the breakage of Si-H bonds and more dangling bonds in a-Si:H(i) bulk or a-Si:H/c-Si interface.<sup>[42–46]</sup> The other one is the porous film cannot stand the ions bombardment during the sputtering, allowing more ions to penetrate the deeper films and causing more metastable defects along the incursion paths in the films.

To clarify where the sputtering damage comes from in this work, ITO was sputtered on the a-Si:H(i)/nc-Si:H(n) passivated sample with different filters placed on top, the detailed layout of which is displayed in **Figure 6a**. The wafer was put into a metal mask before the sputtering process, by which four small squares with an area of  $20 \times 20 \text{ mm}^2$  can be defined. During the ITO



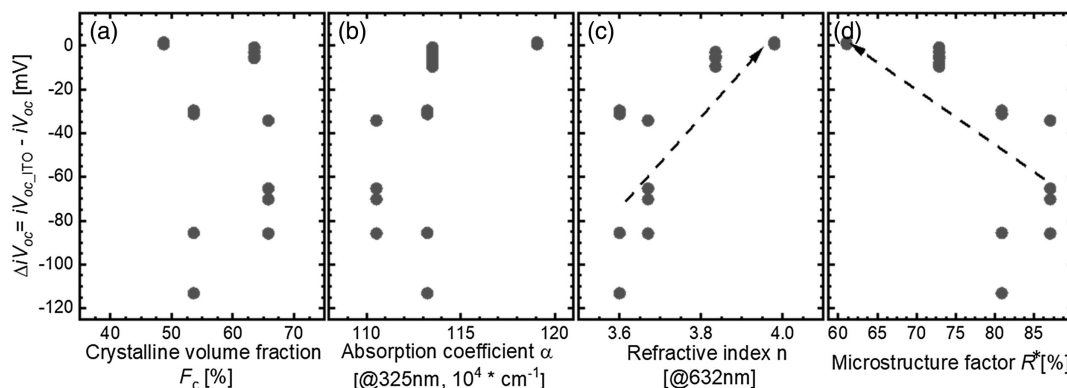


**Figure 5.** The difference of implied open-circuit voltage ( $\Delta V_{oc}$ ) before and after ITO deposition for the devices with different nc-Si:H( $n$ ) layers versus: a) the crystalline volume fraction ( $F_c$ ), b) the absorption coefficient ( $\alpha$ ) at the wavelength of 325 nm, c) the refractive index ( $n$ ) at a wavelength of 632 nm, and d) the microstructure factor ( $R^*$ ). The dashed line works as a guide for the eyes.

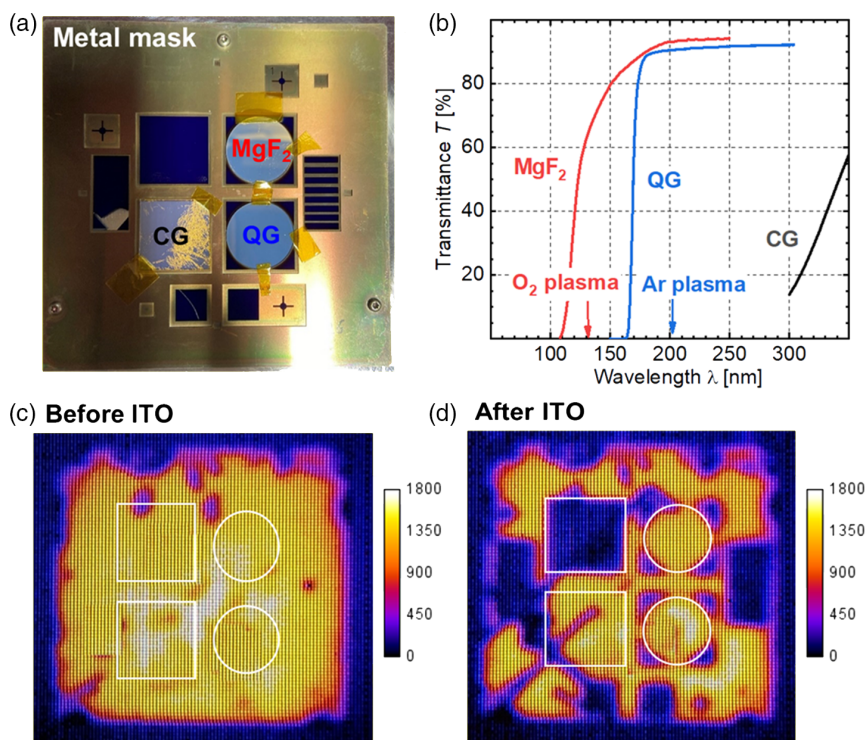


**Figure 6.** a) Layout of the lifetime sample with metal mask and three kinds of filters,  $MgF_2$ , quartz glass (QG), and corning glass (CG), on corresponding positions. b) The transmittance of the filters as a function of the wavelength. The arrow marks locate in the emission peak of  $O_2$  plasma or Ar plasma. The photoluminescence (PL) images of the lifetime sample: c) before and d) after the ITO sputtering process. The position of filters was marked with white circles or rectangles.

deposition, three of them were shielded by filters, using corning glass (CG),  $MgF_2$ , and quartz glass (QG), to distinguish whether the degradation of passivation is from optical radiation or from ion bombardment. The filter excludes ion bombardment and other potential direct reactions of the plasma with the silicon layers. Figure 6b shows the transmittance curves of the different

filters used in this work. The  $MgF_2$  filter blocks the photons with wavelengths below 110 nm ( $>11.3$  eV), whereas it allows a 60% transmittance at the emission peak of 130.5 nm (9.5 eV) related to the oxygen plasma and a 92% transmittance at the emission peak of 210 nm (5.9 eV) associated with the Ar plasma. The cutoff wavelength of the QG filter is 160 nm ( $>7.75$  eV) while it has

90% of transmittance at the emission peak of the Ar plasma.<sup>[18,37]</sup> The usage of the CG could absorb photons with wavelength <250 nm to get rid of the potential degradation induced by VUV and UV radiation. Figure 6c,d shows the photoluminescence (PL) image of the lifetime sample before and after ITO depositions, respectively. A strong sputter damage is observed as expected for the small square without a filter, while no noticeable deterioration of the passivation is found for all the places with a filter. This result reveals that ion bombardment is the dominant reason for the sputtering damage in this work. Compared to the F1, more hydrogen bonded on the inner surface of voids was detected for the F2, which could suffer from a stronger rupture of the Si-H bonds during the ITO sputtering process and promote the deterioration of passivation in the D2.<sup>[36]</sup> Furthermore, the ions with kinetic energies impinging on the nc-Si:H(n) film could displace surface or bulk Si atoms of nc-Si:H or even penetrate the a-Si:H(i) underneath by ion-Si atoms collisions, yielding the generation of metastable defects in the Si network along the ion incursion path in the film.<sup>[14,19,47]</sup> Voids in the network are much easier to be passed through by ions, which could cause a larger injured area in the F2 compared to the F1, giving rise to more severe degradation of the passivation quality.

**Figure 7a** shows the penetration depth of the different atoms with an initial kinetic energy of 270 eV in nc-Si:H(n)/a-Si:H(i) stacks, evaluated via the Stopping and Range of Ions in Matter (SRIM) software based on Monte Carlo simulation method.<sup>[48,49]</sup> The detailed setup of SRIM in this work can be found in Figure S3 (Supporting Information). All ions penetrate the nc-Si:H(n) film and reach the bulk of the passivation layer, whereas the incursion depth of Ar, In, and Sn is smaller than O, which is expected to be the majority element of the negative charge incident on the substrate during the sputtering process.<sup>[38]</sup> A depth of 80 Å within the nc-Si:H(n)/a-Si:H(i) stack for energetic oxygen atoms is demonstrated, which is very close to the a-Si:H/c-Si interface, in good agreement with that reported by Tusch et al.<sup>[19]</sup> There may be a high probability that some stray ions reach the a-Si:H/c-Si interface and cause the deterioration of the surface passivation. Figure 7b shows the oxygen ion distribution in the nc-Si:H(n)/a-Si:H(i) stack when varying the density of nc-Si:H(n). By depositing a denser capping layer upon a-Si:H(i), a reduced spreading depth of O ions in silicon

**Table 2.** The deposition parameters and layer properties of the nc-Si:H(n) layers, namely F2, F3, and F4.

	$f_{\text{SiH}_4}$ [%]	$P$ [W]	$f_{\text{PH}_3}$ [%]	$p$ [mbar]	$\sigma$ [S cm <sup>-1</sup> ]	$F_c$ [%]	$E_{04}$ [eV]	$n$ @632 nm	$R^*$ [%]
F2	0.50	100	4	2.5	27	63.5	2.03	3.82	73
F3	0.50	100	4	3.5	16.1	60.4	1.99	4.0	58
F4	0.50	100	4	4.5	6.8	56.1	1.96	4.1	41

films can be achieved, which could be a sufficient way to relieve the TCO sputtering damage in SHJ solar cells.

### 3.4. Strategy to Reduce Sputter Damage

Research demonstrated that increasing the process pressure during the nc-Si:H deposition gives rise to a reduced microstructure factor of nc-Si:H as well as the intensity in HSM.<sup>[50,51]</sup> Therefore, a variation of the pressure from 2.5 to 4.5 mbar, was carried out to improve the layer density. The detailed deposition parameters and optoelectronic properties of the corresponded nc-Si:H films, namely F2, F3, and F4, are listed in Table 2.

Although a slight decrease of the optical bandgap and crystalline volume fraction is detected at higher deposition pressure, an expected decreased microstructure factor of nc-Si:H(n) films is acquired, accompanied by an increase of the refractive index. This result indicates a denser nc-Si:H(n) film achieved at higher pressure. The detailed deconvolutions of the IR absorption spectrum, refraction index curve, and absorption coefficient curve of these films are plotted in Figure S4 (Supporting Information). Afterward, we applied the optimized nc-Si:H(n) films as an electron-selective layer in rear-junction SHJ solar cells, namely D2, D3, and D4. The QSSPC results of the precursor devices before and after ITO deposition are plotted in Figure 8. All lifetime results before ITO deposition are quite similar, revealing that no noticeable detriment to the passivation quality is found when varying the pressure during the deposition of the n-layer. The drop in the lifetime curve originating from the sputtering processes is reduced by increasing the deposition pressure of nc-Si:H(n) films. Hence, a decreased difference of  $iV_{oc}$  from

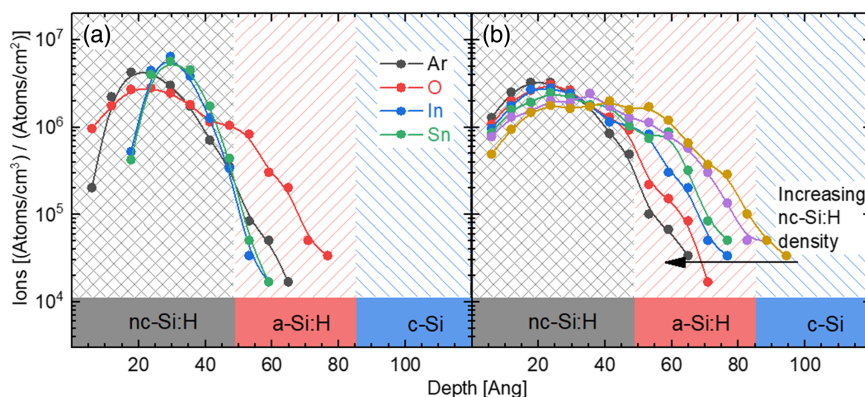


**Figure 7.** Simulated distribution of: a) the different ions involved in sputtering plasma and b) the oxygen ions with an initial kinetic energy of 270 eV in the a-Si:H(i)/nc-Si:H(n) stacks by SRIM Monte Carlo simulation. The properties of nc-Si:H(n) in prior graph were set constant while the density in the later one was tuned by changing the Si/H ratio of the film. The detailed setup of SRIM in this work can be found in Figure S3 (Supporting Information).

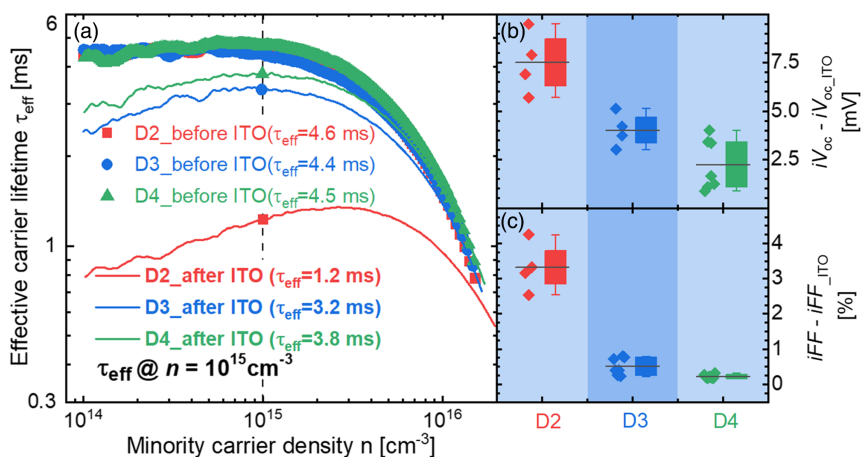


**Figure 8.** a) Effective carrier lifetime ( $\tau_{eff}$ ) versus the minority carrier density ( $n$ ) and the difference of, b) implied open-circuit voltage ( $iV_{oc} - iV_{oc\_ITO}$ ) and c) the implied fill factor ( $iFF - iFF\_ITO$ ) of the precursor devices, D2, D3, and D4, were evaluated by QSSPC lifetime measurement before and after ITO sputtering process. The value of  $\tau_{eff}$  indicated in the graph was determined at the minority carrier density of  $10^{15} \text{ cm}^{-3}$ . The nc-Si:H(n), namely F2, F3, and F4, were used in the D2, the D3, and the D4, respectively, the detailed deposition parameters of which are listed in Table 2. The box plots summarize the statistic of more than 4 samples per group and the line is the median position.

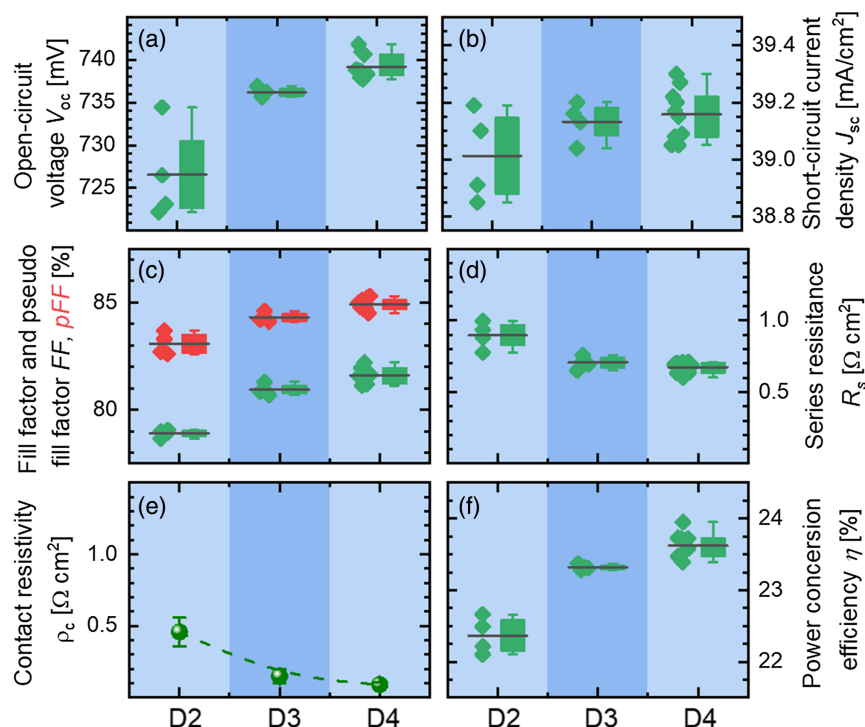


**Figure 9.** a) Open-circuit voltage ( $V_{oc}$ ), b) short-circuit current density ( $J_{sc}$ ), c)  $FF$ ,  $pFF$ , d) series resistance ( $R_s$ ), e) front total contact resistivity ( $\rho_c$ ), and f) power conversion efficiency ( $\eta$ ) of the solar cells, namely D2, D3, and D4. The nc-Si:H(n) layers, namely F2, F3, and F4, were used in the D2, the D3, and the D4, respectively, the detailed deposition parameters of which are listed in Table 2. The box plots summarize the statistic of more than 4 samples per group and the line is the median position.

7.5 to 2.5 mV and  $iFF$  from 3.5 to 0.3%<sub>abs</sub> is noted in Figure 8b,c, respectively. This result demonstrates the success of the strategy to release the sputtering damage by using a denser capping layer with lower defect density.

The final cell performance of the devices with different nc-Si:H(n) layers is displayed in Figure 9. The average  $V_{oc}$  of the D4 increased by 12 mV compared with the S2. This improvement originates from the aforementioned decrease in sputter

damage. A slight gain of  $J_{sc}$  is achieved when using denser nc-Si:H(n) layers, which is contrary to the optical properties shown in Table 2. It could be explained by the improvement of the carrier transport and collection in the silicon bulk due to the reduction of the front surface recombination. This interpretation is demonstrated by the increased IQE in the range between 600 and 1000 nm, as shown in Figure S5 (Supporting Information). More apparently, a dramatic increase of FF from 79% to 81.5% and  $pFF$  from 83% to 85% are found in Figure 9c as varying the nc-Si:H(n) layer from F2 to F4, which is the benefit of the reduced sputter damage. Furthermore, a lower  $R_s$  is also obtained in the D4 compared with the other devices, suggesting a reduced resistive loss and an enhanced charge carrier transport due to the denser nc-Si:H(n) layer with lower defect density. This hypothesis is verified by the reduced contact resistivity between ITO and nc-Si:H(n) from 0.48 to 0.1  $\Omega\text{cm}^2$  in Figure 9e as increasing the deposition pressure of nc-Si:H(n), which still has room to be further reduced in comparison with the result reported by Long et al.<sup>[52]</sup> Finally, an enhancement of the average power conversion efficiency from 22.4% to 23.6% is acquired. The best solar cell in this work exhibits  $V_{oc}$  of 741.8 mV, FF of 82.2%,  $J_{sc}$  of 39.27  $\text{mA cm}^{-2}$  and  $\eta$  of 23.95% on the M2-sized wafer. Additionally, this cell was selected to be certificated at ISFH CalTec (Hamelin, Germany) and the measured IV parameters are represented in Figure S6 (Supporting Information), showing a total area efficiency of  $23.87 \pm 0.36\%$ .

## 4. Conclusion

In this article, we observed TCO sputter damage in the rear-junction SHJ solar cells with ultra-thin (5 nm) n-type nc-Si:H layers and demonstrated a strategy to reduce it by increasing the density of nc-Si:H film. PL images demonstrate that ion bombardment is the dominant reason for the sputtering damage on nc-Si:H. Estimated by SRIM simulation, the ions with an initial kinetic energy of 270 eV are able to penetrate the 5 nm nc-Si:H(n) protective layer, which may modify the underlying silicon thin films or the a-Si:H/c-Si interface. The voids in nc-Si:H thin film could provide a channel for the transport of the energetic ions in the ITO sputtering plasma, resulting in the generation of metastable defects along the ion incursion path in the films. By using a denser nc-Si:H(n), a decreased sputter damage was demonstrated, resulting in an enhancement of the average power conversion efficiency from 22.4% to 23.6%. The best solar cell (area 244  $\text{cm}^2$ , on an M2-sized wafer) exhibits a  $V_{oc}$  of 741.8 mV, FF of 82.2%,  $J_{sc}$  of 39.27  $\text{mA cm}^{-2}$ , and an efficiency  $\eta$  of 23.95%. The sputter damage issue on nc-Si:H by TCO has been explored for the first time from the perspective of silicon thin films, which gives a diversified strategy for the application of nc-Si:H in SHJ solar cells.

## Supporting Information

Supporting Information is available from the Wiley Online Library or from the author.

## Acknowledgements

The authors would like to thank Hildegard Siekmann for the ITO sputtering, Alain Doumit and Henrike Gattermann for the wafer texture and cleaning, Henrike Gattermann and Iris Caspers for the screen printing, Silke Lynen, Volker Lauterbach, Andreas Mück, Andreas Schmalen, Johannes Wolff, Daniel Weigand, and Wilfried Reetz for the technical assistance. This work was supported by the German Federal Ministry of Economic Affairs and Energy in the framework of the STREET project (grant: 0324275E), TUKAN project (grant: 0324198D), TOUCH project (grant: 0324351), and the (HEMF) Helmholtz Energy Materials Foundry infrastructure funded by the HGF (Helmholtz association). The authors are grateful for the financial support from China Scholarship Council (No. 201706380037) and the wafers supply by LONGI company.

Open Access funding enabled and organized by Projekt DEAL.

## Conflict of Interest

The authors declare no conflict of interest.

## Data Availability Statement

The data that support the findings of this study are available from the corresponding author upon reasonable request.

## Keywords

nanocrystalline silicon, silicon heterojunction solar cells, sputter damage

Received: July 18, 2022

Revised: August 10, 2022

Published online: August 25, 2022

- [1] J. Haschke, O. Dupré, M. Boccard, C. Ballif, *Sol. Energy Mater. Sol. Cells* **2018**, 187, 140.
- [2] S. DeWolf, A. Descoedres, Z. C. Holman, C. Ballif, *Green* **2012**, 2, 7.
- [3] PV Magazine, *Longi's Heterojunction Solar Cell Hits 26.5%*, <https://www.pv-magazine.com/2022/06/24/longis-heterojunction-solar-cell-hits-26-5/>, (accessed: June 2022).
- [4] A. Richter, L. Zhao, F. Finger, K. Ding, *Surf. Coat. Technol.* **2016**, 295, 119.
- [5] O. Vetterl, F. Finger, R. Carius, P. Hapke, L. Houben, O. Kluth, A. Lambert, A. Mück, B. Rech, H. Wagner, *Sol. Energy Mater. Sol. Cells* **2000**, 62, 97.
- [6] F. Finger, P. Hapke, M. Luysberg, R. Carius, H. Wagner, M. Scheib, *Appl. Phys. Lett.* **1994**, 65, 2588.
- [7] M. Sharma, J. Panigrahi, V. K. Komarala, *Nanoscale Adv.* **2021**, 3, 3373.
- [8] G. Nogay, J. P. Seif, Y. Riesen, A. Tomasi, L. Barraud, N. Wyrsh, F. J. Haug, S. De Wolf, C. Ballif, in *2017 IEEE 44th Photovolt. Spec. Conf. PVSC 2017* **2017**, Vol. 6, p. 13, <https://doi.org/10.1109/PVSC.2017.8366840>.
- [9] H. Overhof, M. Otte, M. Schmidtke, U. Backhausen, R. Carius, *J. Non-Cryst. Solids* **1998**, 227–230, 992.
- [10] A. V. Shah, J. Meier, E. Vallat-Sauvain, N. Wyrsh, U. Kroll, C. Droz, U. Graf, *Sol. Energy Mater. Sol. Cells* **2003**, 78, 469.
- [11] D. Qiu, W. Duan, A. Lambert, K. Bittkau, P. Steuter, Y. Liu, A. Gad, M. Pomaska, U. Rau, K. Ding, *Sol. Energy Mater. Sol. Cells* **2020**, 209, 110471.
- [12] K. Ding, U. Aeberhard, V. Smirnov, B. Holländer, F. Finger, U. Rau, *Jpn. J. Appl. Phys.* **2013**, 52, 122304.



- [13] S. Nunomura, I. Sakata, K. Matsubara, *Phys. Rev. Appl.* **2018**, *10*, 054006.
- [14] A. Illiberi, P. Kudlacek, A. H. M. Smets, M. Creatore, M. C. M. Van De Sanden, *Appl. Phys. Lett.* **2011**, *98*, 10.
- [15] A. H. T. Le, V. A. Dao, D. P. Pham, S. Kim, S. Dutta, C. P. Thi Nguyen, Y. Lee, Y. Kim, J. Yi, *Sol. Energy Mater. Sol. Cells* **2019**, *192*, 36.
- [16] B. Macco, H. C. M. Knoops, W. M. M. Kessels, *ACS Appl. Mater. Interfaces* **2015**, *7*, 16723.
- [17] B. Demareux, J. P. Seif, S. Smit, B. MacCo, W. M. M. E. Kessels, J. Geissbuhler, S. De Wolf, C. Ballif, *IEEE J. Photovoltaics* **2014**, *4*, 1387.
- [18] Y. Kuang, B. Macco, B. Karasulu, C. K. Ande, P. C. P. Bronsveld, M. A. Verheijen, Y. Wu, W. M. M. Kessels, R. E. I. Schropp, *Sol. Energy Mater. Sol. Cells* **2017**, *163*, 43.
- [19] D. Qiu, W. Duan, A. Lambertz, K. Bittkau, K. Qiu, U. Rau, K. Ding, *Sol. Energy* **2022**, *231*, 578.
- [20] L. Tutsch, M. Bivour, W. Wolke, M. Hermle, J. Rentsch, in *33rd Eur. PV Sol. Energy Conf. Exhib.* **2017**, <https://doi.org/10.1109/JPHOTOV.2015.2484962>.
- [21] M. Semma, K. Gotoh, M. Wilde, S. Ogura, Y. Kurokawa, K. Fukutani, N. Usami, *AIP Adv.* **2020**, *10*, 065008.
- [22] D. Qiu, W. Duan, A. Lambertz, Z. Wu, K. Bittkau, K. Qiu, Z. Yao, U. Rau, K. Ding, *ACS Appl. Energy Mater.* **2021**, *4*, 7544.
- [23] R. A. Sinton, A. Cuevas, in *16th Eur. Photovolt. Sol. Energy Conf.* **2000**, pp. 1–4, <https://doi.org/citeulike-article-id:6901946>.
- [24] W. Duan, A. Lambertz, K. Bittkau, D. Qiu, K. Qiu, U. Rau, K. Ding, *Prog. Photovoltaics Res. Appl.* **2021**, *30*, 384.
- [25] Z. Yao, W. Duan, P. Steuter, J. Hüpkens, A. Lambertz, K. Bittkau, M. Pomaska, D. Qiu, K. Qiu, Z. Wu, H. Shen, U. Rau, K. Ding, *Sol. RRL* **2021**, *5*, 2000501.
- [26] D. Qiu, W. Duan, A. Lambertz, K. Bittkau, K. Qiu, K. Ding, in *Conf. Rec. IEEE Photovolt. Spec. Conf.* **2021**, pp. 806–808, <https://doi.org/10.1109/PVSC43889.2021.9518937>.
- [27] M. Hermle, F. Granek, O. Schultz, S. W. Glunz, *J. Appl. Phys.* **2008**, *103*, 054507.
- [28] T. Kaneko, D. Nemoto, A. Horiguchi, N. Miyakawa, *J. Cryst. Growth* **2005**, *275*, 1097.
- [29] D. M. Goldie, S. K. Persheyev, *J. Mater. Sci.* **2006**, *41*, 5287.
- [30] A. A. Langford, M. L. Fleet, B. P. Nelson, W. A. Lanford, N. Maley, *Phys. Rev. B* **1992**, *45*, 13367.
- [31] Z. Wu, W. Duan, A. Lambertz, D. Qiu, M. Pomaska, Z. Yao, U. Rau, L. Zhang, Z. Liu, K. Ding, *Appl. Surf. Sci.* **2021**, *542*, 16.
- [32] M. Fecioru-Morariu, B. Mereu, J. Kalas, J. Hoetzel, P. A. Losio, M. Kupich, O. Kluth, T. Eisenhammer, in *EU-PVSEC Proc.* **2010**, pp. 2947–2950.
- [33] J. Müllerová, P. Šutta, G. van Elzakker, M. Zeman, M. Mikula, *Appl. Surf. Sci.* **2008**, *254*, 3690.
- [34] E. Bhattacharya, A. H. Mahan, *Appl. Phys. Lett.* **1988**, *52*, 1587.
- [35] M. Stuckelberger, R. Biron, N. Wyrsh, F. J. Haug, C. Ballif, *Renewable Sustainable Energy Rev.* **2017**, *76*, 1497.
- [36] B. Demareux, S. De Wolf, A. Descoedres, Z. Charles Holman, C. Ballif, *Appl. Phys. Lett.* **2012**, *101*, 171604.
- [37] H. B. Profijt, P. Kudlacek, M. C. M. van de Sanden, W. M. M. Kessels, *J. Electrochem. Soc.* **2011**, *158*, G88.
- [38] T. Welzel, K. Ellmer, *Vak. Forsch. Prax.* **2013**, *25*, 52.
- [39] C. Böhm, J. Perrin, P. Roca I Cabarrocas, *J. Appl. Phys.* **1993**, *73*, 2578.
- [40] H. D. Hagstrum, *Phys. Rev.* **1954**, *96*, 336.
- [41] J. Dubeau, L. Hamel, T. Pochet, *Phys. Rev. B* **1996**, *53*, 10740.
- [42] S. De Wolf, B. Demareux, A. Descoedres, C. Ballif, *Phys. Rev. B* **2011**, *83*, 233301.
- [43] K. Eriguchi, *Jpn. J. Appl. Phys.* **2017**, *56*, 06HA01.
- [44] P. Mahtani, R. Varache, B. Jovet, C. Longeaud, J. P. Kleider, N. P. Kherani, *J. Appl. Phys.* **2013**, *114*, 124503.
- [45] M. Stutzmann, W. B. Jackson, C. C. Tsai, *Phys. Rev. B* **1985**, *32*, 23.
- [46] H. Plagwitz, B. Terheiden, R. Brendel, *J. Appl. Phys.* **2008**, *103*, 094506.
- [47] A. H. M. Smets, W. M. M. Kessels, M. C. M. Van De Sanden, *J. Appl. Phys.* **2007**, *102*, 073523.
- [48] J. F. Ziegler, M. D. Ziegler, J. P. Biersack, *Nucl. Instrum. Methods Phys. Res., Sect. B* **2010**, *268*, 1818.
- [49] J. F. Ziegler, J. P. Biersack, M. D. Ziegler, *The Stopping and Range of Ions in Matter* **2008**, p. 8.1–8.19.
- [50] Y. Wang, H. Liu, W. Shen, *Nanoscale Res. Lett.* **2018**, *13*, 234.
- [51] S. Ray, S. Mukhopadhyay, *Philos. Mag.* **2009**, *89*, 2573.
- [52] W. Long, S. Yin, F. Peng, M. Yang, L. Fang, X. Ru, M. Qu, H. Lin, X. Xu, *Sol. Energy Mater. Sol. Cells* **2021**, *231*, 111291.